TU Delft

Delft University of Technology

Document Version
Final published version

Licence
CC BY

Citation (APA)
Blom, Y., Santbergen, R., Isabella, O., & Vogt, M. R. (2026). Investigating the energy yield performance of smart photovoltaic modules in shaded environments. *Solar Energy*, *317*, Article 114992. https://doi.org/10.1016/j.solener.2026.114992

Important note
To cite this publication, please use the final published version (if applicable).
Please check the document version above.

Copyright
In case the licence states “Dutch Copyright Act (Article 25fa)”, this publication was made available Green Open Access via the TU Delft Institutional Repository pursuant to Dutch Copyright Act (Article 25fa, the Taverne amendment). This provision does not affect copyright ownership.
Unless copyright is transferred by contract or statute, it remains with the copyright holder.

Sharing and reuse
Other than for strictly personal use, it is not permitted to download, forward or distribute the text or part of it, without the consent of the author(s) and/or copyright holder(s), unless the work is under an open content license such as Creative Commons.

Takedown policy
Please contact us and provide details if you believe this document breaches copyrights.
We will remove access to the work immediately and investigate your claim.

This work is downloaded from Delft University of Technology.

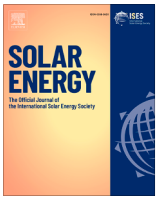
Solar Energy 317 (2026) 114992



Contents lists available at ScienceDirect

Solar Energy

journal homepage: www.elsevier.com/locate/solener





Investigating the energy yield performance of smart photovoltaic modules in shaded environments

Youri Blom*, Rudi Santbergen, Olindo Isabella, Malte Ruben Vogt*

Delft University of Technology, Mekelweg 4, Delft, 2628CD, the Netherlands

HIGHLIGHTS

- Smart modules outperform butterfly modules in urban environments due to improved shade resilience.
- Smart modules reduce the maximum temperatures due to fewer reverse bias operations.
- Smart modules can tolerate up to 50% additional module costs for similar LCOE values.
- Reverse bias behavior has a trade-off between energy yield and cell temperatures.

ARTICLE INFO

Keywords:
Smart PV modules
Energy yield modeling
Partial shading
Degradation modeling
Reverse bias operation

ABSTRACT

In urban settings, residential photovoltaic (PV) systems typically involve conversion from direct to alternating current either at the string or module level. Generally, conversion at the module level offers better performance in shading scenarios induced by the built environment but is usually more expensive. This study explores the potential of 'Smart' PV modules, which include built-in buck converters that allow substrings within a PV module to operate independently and thus improve PV energy yield in shaded urban scenarios. Eight PV system configurations, varying in inverter topology and cell architecture, are simulated across three locations. Results show that systems using string inverters with Smart modules achieve the highest annual energy yield. Financial analysis further demonstrates that for the considered scenario's up to 50% additional module costs are tolerable for a similar financial performance. In addition to energy yield improvements, Smart modules reduce the maximum temperatures observed within the system.

1. Introduction

The deployment of photovoltaic (PV) systems in urban areas can significantly contribute to meeting urban energy demands while enhancing sustainability and energy independence [1–3]. In 2024, about 40% of the total PV system capacity in the Netherlands is installed on homes [4] and those residential PV systems accounted for 7.2% of the electricity generation in the Netherlands [5]. These systems typically handle the conversion from direct to alternating current on either central, string or module level, with the latter two being preferred for residential applications [6]. One of the major challenges faced by PV systems in urban environments is partial shading, which not only negatively impacts power production [7], but also increases the module temperature of the PV module [8], potentially leading to hotspot failures [9].

Various studies have investigated this behavior and compared the performance of string and microinverters, revealing that microinverters generally achieve better performance in residential PV systems [6,10]. This advantage is primarily because microinverters allow each module to operate at its own maximum power point (MPP). However, microinverters come with higher costs compared to string inverters [11,12]. This contributes to the fact that the levelized cost of electricity (LCOE) of a rooftop PV system is significantly higher than that of a utility scale PV system [13].

An approach to address this problem is to utilize power optimizers in combination with string inverters [14–16]. This way, power optimizers allow all modules to operate at their own MPP, while inverters are only needed at the string level, thereby reducing the LCOE. However, this approach still suffers from mismatches between cells in the same module, as the power optimizers operate at the module level.

* Corresponding authors.
Email addresses: Y.Blom@tudelft.nl (Y. Blom), M.R.Vogt@tudelft.nl (M.R. Vogt).

https://doi.org/10.1016/j.solener.2026.114992
Received 25 February 2026; Received in revised form 31 July 2026; Accepted 1 August 2026
Available online 6 August 2026
0038-092X/© 2026 The Author(s). Published by Elsevier Ltd on behalf of International Solar Energy Society. This is an open access article under the CC BY license (http://creativecommons.org/licenses/by/4.0/).

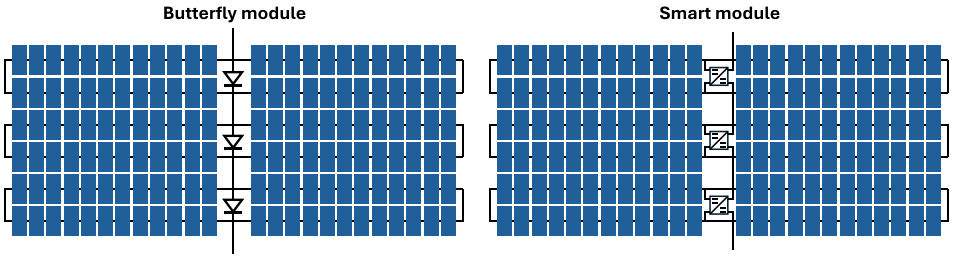


Fig. 1. An overview of the different modules considered. The archetype of butterfly topology (left-hand side) constitutes the basis of the Smart PV module topology (right-hand side). The latter is equipped with buck converters, allowing the substrings to operate at their own maximum power point.

The robustness against mismatches at the cell level can already be improved by using a butterfly layout, as shown in Fig. 1. This layout creates two substrings in parallel, making the module more shade resilient in case shading occurs on one side of the module [17].

To further improve the shade resilience and reduce the LCOE of residential PV systems, string inverters can be combined with shade-tolerant PV modules, offering a more cost-effective solution. In the literature, various studies have developed different strategies for improving the shade tolerance of PV modules. Mathews et al. provided an overview of different partial shading mitigation techniques, such as bifacial PV panels and cleaning techniques [18]. Another approach is to use the small-area-high-voltage concept as proposed by Fauzan et al. [19,20], which demonstrated higher shading tolerability compared to conventional PV modules. Furthermore, it is possible to integrate power electronics into PV modules to improve shade resilience [21–23], as integrated power electronics play an important role in a wide range of renewable energy sources [24]. Calcabrini et al. proposed a fully reconfigurable photovoltaic module that can boost the energy yield by over 12% under partial shading [25]. Another approach comes from Stauth et al., who proposed using resonant switched-capacitor converters on the submodule level to improve performance during partial shading [26]. Similarly, Mirbagheri Golroodbari et al. introduced and demonstrated a design in which the traditional bypass diodes in PV modules are replaced with buck converters [27,28]. This enables all substrings within a module to operate at their own MPP while remaining connected to a string inverter, reaching a higher level of granularity. This enhances the PV modules' resilience to partial shading without requiring proprietary inverter technology. We will refer to this last design of Mirbagheri Golroodbari et al. as a *Smart module*. Such smart modules are also commercially available [29].

In this work, we study the full potential of these Smart modules by simulating the outdoor performance of various PV systems. In total, four inverter topologies are considered, which are Butterfly modules with string inverters (String), butterfly modules with micro inverters (Micro), butterfly modules with string inverters and power optimizers (String + Power), and Smart modules with string inverters (String + Smart). It should be realized that the Micro-system and String + Power-system have a very similar electrical performance, as both systems allow modules to operate independently. A detailed comparison between these two topologies is provided in Appendix A. For completeness, both topologies are included in the comparison.

Regarding the cell design, we analyze PV systems featuring Tunnel Oxide Passivated Contact (TOPCon) cells in either Interdigitated Back Contact (IBC) or Front/Back Contact (FBC) architecture. By combining these configurations, a total of eight distinct PV system designs are examined.

The performance of each system is evaluated based on annual electricity generation across three locations to assess shade resilience. Additionally, we analyze temperature data for all cells throughout the year to determine the maximum temperatures reached in the different scenarios. Finally, we assess how module topology affects the power loss due to degradation.

2. Methodology

All simulations employ the PVMD Toolbox [30,31], a modeling framework for PV systems that calculates energy yield by sequentially modeling diverse meteorological, optical, geometrical, and electro-thermo-mechanical aspects. The calculations are carried out on the Delft High Performance Computing Centre [32]. First, the optical response of the PV module is simulated, also accounting for shading effects due to surrounding objects. Next, the received irradiance is determined using hourly weather data. This is followed by the thermal simulation, which calculates the temperature of each cell in the PV modules forming the PV system throughout the year. Both irradiance and temperature data serve as inputs for the electrical simulation, which quantifies the generated DC electricity. As the thermal performance of a solar cell is affected by its electrical operating point, an iterative calculation between the thermal and electrical models is used to accurately simulate the thermo-electrical behavior of the solar cell. Finally, conversion losses are incorporated to determine the total AC electricity output. A detailed description of this methodology is available in previous work [30,31,33].

In the rest of this section, we will discuss important assumptions and specifications needed to understand the results of this work. This includes the module layout, received irradiance, electrical cell performance, conversion modeling, and economic modeling. The section ends with a validation of the iterative thermal-electrical calculation.

2.1. Module layout

The modules under consideration are equipped with half-cut wafers measuring 156 × 78 mm, consistent with the cell dimensions to fit the shading situation used in a previous study [34]. These cells are arranged in a butterfly topology, where they are divided into six substrings and bypass diodes are connected, as illustrated in Fig. 1. Previous studies have shown that this topology offers greater resilience to shading compared to the conventional series-connected configuration [35].

For the Smart modules, the bypass diodes are replaced with buck converters. The functionality and implementation of the Smart module were discussed in previous work [31].

2.2. Received irradiance

The irradiance received by each cell within the PV system is based on a study conducted by Calcabrini et al. [34]. The analysis considers a rooftop with multiple objects and 25 PV modules, as illustrated in Fig. 2(a), which is facing southwest with an angle of 146° from the north. Fig. 2(b) illustrates with color which modules are connected together when a string inverter is considered. The modules are divided over two string inverters, as the cumulative voltage of all modules would exceed the voltage rating of the selected inverter. The comparison of inverter topologies is conducted for the following three locations: Rotterdam (the Netherlands), Bogotá (Colombia), and San Francisco (USA). For each location, the study by Calcabrini et al. provides the irradiance data for each cell within the PV system at a 10-minute resolution. The total received irradiance for all cells in the PV system at each location is shown

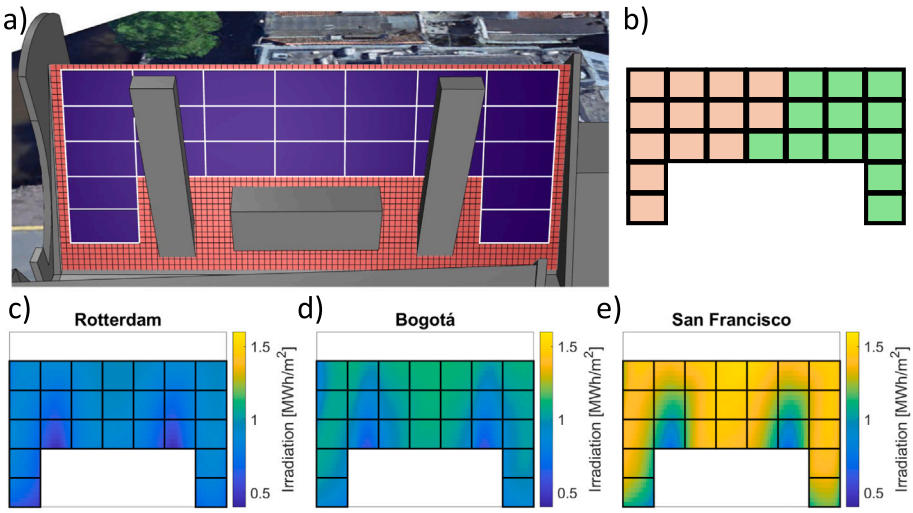


Fig. 2. (a) an image of the considered roof with installed PV modules, and (b) the module interconnection of the PV system with a string inverter. The other pictures show the annual irradiation received in Rotterdam (c), Bogotá (d) and San Francisco (e).

at the bottom of Fig. 2. These irradiances are used as input for the thermal and electrical modeling to calculate cell temperatures and generated DC power.

It should be realized that this work only considers one rooftop, and that the results from this work cannot automatically be generalized for all urban environments. However, it is very difficult to design a rooftop that is representative of all locations, as this heavily differs between countries. The considered rooftop, which is based on an actual building [34], is chosen as it can be used to understand the difference in performance between the considered PV systems in a real-world case study. Future work and more case studies are needed to prove that the findings of this work are generalizable to all urban environments.

2.3. Electrical cell modeling

The modeling of electrical performance at the cell level is separated into forward and reverse bias behavior for both IBC-based and FBC-based modules, while considering the differences in the cell architectures.

2.3.1. Forward bias

For forward bias conditions, we use a Calibrated Lumped Element Method (CLEM) model, as detailed in [30]. This model consists of a photocurrent source (J_{ph}), a diode, a shunt resistance (R_{sh}) accounting for leakage losses, and a series resistance (R_s) representing ohmic losses.

To ensure the electrical performance reflects state-of-the-art PV modules, we calibrate the CLEM model using datasheets from a 22.5% efficient FBC TOPCon module [36] and a 22.8% efficient IBC TOPCon module [37]. Fig. 3 presents the active area current density (JV) curve of both cell architectures under standard test conditions (STC), including the electrical characteristics.

It should be noted that the efficiencies in Fig. 3 do not match the values in the datasheet, as the figure shows the active area efficiency and does not include cell spacing losses. To validate the electrical simulation at forward bias, the IV curves are reconstructed for the same module sizes as those in the datasheet in Appendix B.

2.3.2. Reverse bias

For reverse bias conditions, we utilize the model proposed by Alonso-Garcia et al. [38]. This model expresses the output current under reverse bias as

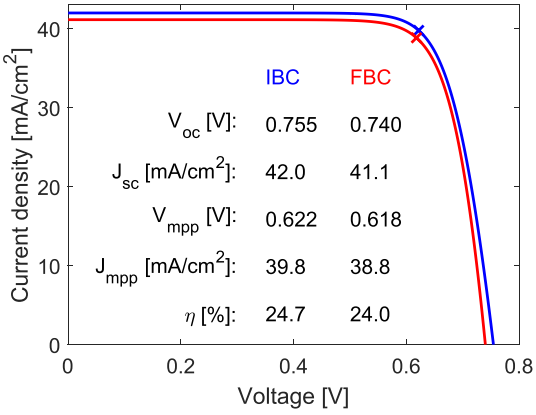


Fig. 3. The electrical performance of both cell architectures in forward bias, including the IV characteristics. The MPP of each cell is indicated with a cross.

$$J(V) = \frac{J_{ph} - \frac{R_{sh} \cdot V + c \cdot V^2}{A}}{1 - \exp\left(B_e \left(1 - \sqrt{\frac{\phi_T - V_b}{\phi_T - V}}\right)\right)}, \quad (1)$$

where c is a coefficient that characterizes the parabolic behavior of the current, A is the area, B_e is a quasi-constant parameter, ϕ_T is the built-in junction voltage, and V_b is the breakdown voltage [38].

These parameters (c, B_e, ϕ_T, and V_b) are fitted using measured reverse bias of an FBC [39] and a IBC cell [40], while J_{ph} and R_{sh} are derived from the electrical behavior at forward bias. Fig. 4 shows the electrical behavior at reverse bias of the cell architectures, including the values of the fitted parameters. As can be seen, the IBC cell has a significantly lower breakdown voltage than the FBC cell.

2.4. Conversion modeling

To obtain the AC electricity, the SNL model [41] is used for the string and micro inverter. This model expresses the AC output power as a function of input voltage and power, incorporating various empirical parameters. These empirical parameters are extracted for both a

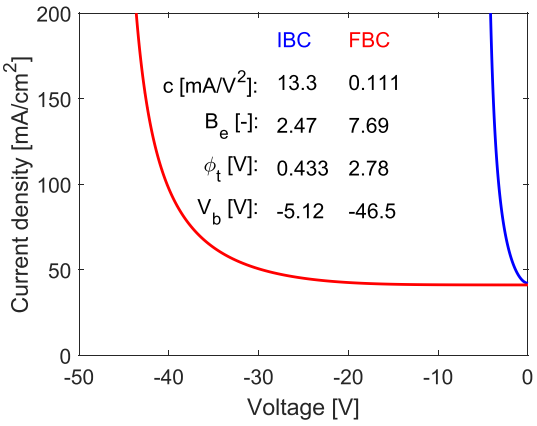


Fig. 4. The electrical performance of both cell architectures in reverse bias, including the fitted parameters.

micro and string inverter, considering two datasheets ([42,43], respectively). Fig. 5(b) and (c) present the efficiency curves of both inverters. For the micro-inverter, we compare the simulated efficiencies with the measured efficiencies. As the datasheet of the string inverter did not provide measured efficiency curves, we compare our EU weighted efficiency with the reported value, showing good agreement.

Converters cannot operate at any input voltage, but require a minimum voltage. As specified by their datasheets, the minimum voltage of the micro and string inverter is 25 V [42] and 140 V [43], respectively.

For the power optimizer, the datasheet from SolarEdge, and the corresponding efficiency curves, are used [44]. Fig. 5(c) shows the efficiency at different input voltages. To validate the implementation of the power optimizer, we compare our EU weighted efficiency with the reported value, which also shows good agreement.

2.5. Economical modeling

The financial performance of all considered systems is quantified using the LCOE, as it represents the levelized costs per unit of generated electricity. In this work, the LCOE is calculated with

$$LCOE = \frac{CAPEX + \sum_{t=1}^{N_{years}} \frac{OPEX(t)}{(1+r)^t}}{\sum_{t=1}^{N_{years}} \frac{EY(t)}{(1+r)^t}}, \quad (2)$$

where $CAPEX$ denotes the capital expenditure (including module, inverter and other costs), $OPEX(t)$ represents the operation and maintenance expenditure in year t, N_{years} is the lifetime of the system, r is the discount rate, and $EY(t)$ is the system energy yield in year t.

Table 1
The assumed values of the parameters for the calculation of the LCOE.

Component	Value	Source
Modules [USD/kWp]	260	IRENA [45]
Increased cost smart modules	varying [%]	
String inverter [USD/unit]	668	Elektrototaalmarkt [46]
Micro inverter [USD/unit]	132	Enphase [47]
Power optimizer [USD/unit]	51	SolarEdge [44]
Other CAPEX [USD/kWp]	773	Kost et al. [13]
OPEX [USD/kWp/year]	30	Kost et al. [13]
Discount rate [%]	5	
System lifetime [years]	25	

The values for all parameters are listed in Table 1. It should be noted that these values may vary significantly across different locations. However, performing a detailed, location-specific cost analysis is beyond the scope of this work. Nevertheless, the selected assumptions are sufficient to quantify the extent to which Smart modules can improve the financial performance of a residential PV system.

2.6. Validation

The performance of the PVMD Toolbox has already been validated in previous work [30,31] in different aspects, such as optical, irradiance, and electrical modeling. One aspect in which validation can be improved is the thermal modeling, with specific focus on the iterative simulation between the thermal and electrical steps. To demonstrate the gain in accuracy by iterating between the thermal and electrical calculations, we use the dataset from the blind modeling comparison conducted by Sandia National Laboratories [48].

Fig. 6 shows the measured temperature of an in-field PV module, and the simulated temperature with and without iteration for two different days. It can be seen that iterative simulation between the thermal and electrical simulation steps significantly improves the accuracy. The overall root mean square (RMS) error, taken over the full year, reduces from 4 °C to 3 °C.

3. Results

The performance of the eight different system topologies is simulated and compared in various aspects. First, a test scenario with partial shading is considered to evaluate the shade-robustness of the Smart modules. Then, the outdoor performance is analyzed to compare the energy yield, maximum temperature, and degradation rates of the different PV systems. Lastly, we also compute the energy yield after 20 years of degradation.

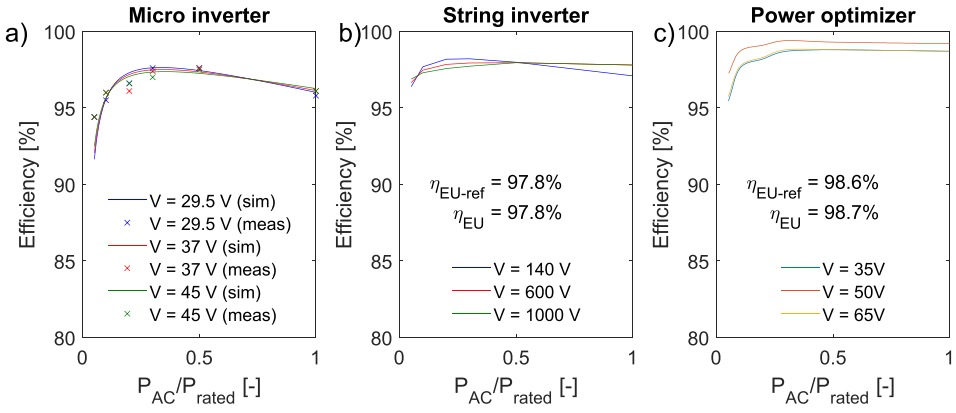


Fig. 5. The efficiency curves for the micro (a) and string (b) inverters at different voltages.

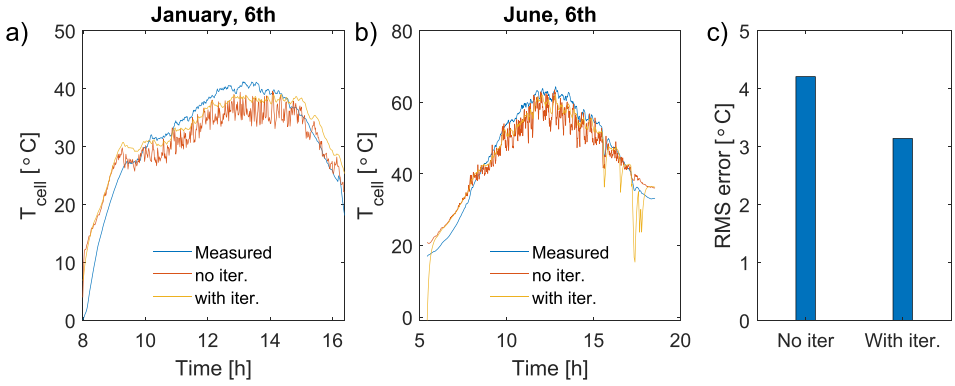


Fig. 6. A comparison between the measured cell temperature and the temperature modelled with and without iterative calculation for a day in January (a) and June (b). Overall, the RMS error reduces from approximately 4 °C to 3 °C (c).

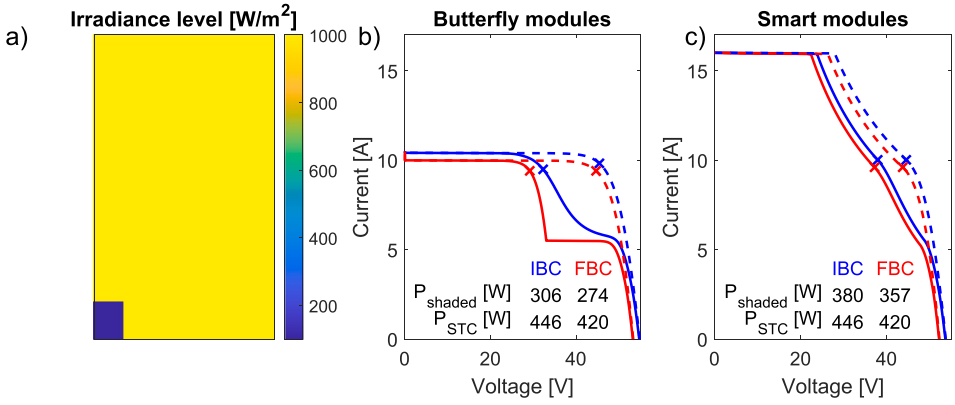


Fig. 7. The IV curves of the different modules under a partial shading scenario. (a) shows the considered irradiance scenario. (b) and (c) show the IV curves of the butterfly and Smart modules, respectively. In each IV curve, the MPP is indicated with a cross. For (b) and (c), the IV curve under normal STC conditions is also shown with dashed lines.

3.1. Test scenarios

Before analyzing the outdoor performance of the different systems, we first consider a test scenario at the module level to compare their performances. In this scenario, the entire module receives an irradiance of 1000 W m^{-2}, except for two cells in the bottom left corner, which receive an irradiance of 100 W m^{-2} (Fig. 7a). The IV curves of the butterfly and Smart modules, using both cell technologies, are shown in Fig. 7(b) and (c). Additionally, the module IV curve under STC conditions is indicated with dashed lines.

The effect of partial shading is clearly visible in the IV curves of the butterfly module (Fig. 7b). The IV curve has two local maxima: one where the bypass diode is activated and one where it is not. Additionally, the lower reverse bias voltage for IBC cells results in a smoother transition between the two local maxima. Under this partially shaded scenario, the IBC and FBC butterfly modules have maximum output powers of 306 W and 274 W, respectively, compared to their normal STC output powers of 446 W and 420 W.

The Smart modules are more robust against partial shading, as shown in Fig. 7(c). The output powers of these smart modules are 380 W and 357 W for the IBC and FBC technologies, respectively, showing an increase of more than 20% (70 W) in maximum output power for both cell architectures, when comparing the butterfly and smart modules. This increase is due to the Smart modules enabling different substrings to operate at their individual maximum power points.

To better illustrate how module IV curves are formed by the submodules, Appendix C shows the IV curves at the submodule level. This demonstrates the effect of the cell architecture and module type on the IV curves.

3.2. Energy yield

To compare the outdoor performance of the different designs, for each PV system, the annual AC output power is calculated for three different locations. Fig. 8 shows the AC energy yield of all eight systems across these locations. It is evident that the systems with Smart modules have the highest energy yield in all locations, showing a 15%–20% gain in energy yield when compared to only string inverters, and a 2%–3% higher energy yield when compared to micro inverters or power optimizers. This is due to their higher robustness against partial shading, as shown in Fig. 7. Furthermore, it can be seen that the systems in San Francisco have the highest energy yield, as this location receives the most irradiance (Fig. 2).

Among all converter topologies, the difference between only string inverters and the rest is much greater than the other differences. This is because the difference in irradiance is much greater between modules within a system than between cells within a module, as shown in Fig. 2. Therefore, allowing a module to operate at its own maximum power point already significantly reduces mismatch losses. Nevertheless, systems with Smart modules still outperform micro-inverter systems as they reduce the level of independence from module to substring.

To better analyze the operational differences between the system with Smart modules and the other configurations, both the annual relative gain per cell and the time-dependent relative gain are quantified. As similar trends are observed across all locations, only the results for Rotterdam are discussed. Fig. 9(a) shows the annual relative gain per cell for the system with Smart modules compared to the other systems. It should be noted that the cell technology is kept identical for this comparison. The relative gain is calculated by dividing the annual electricity

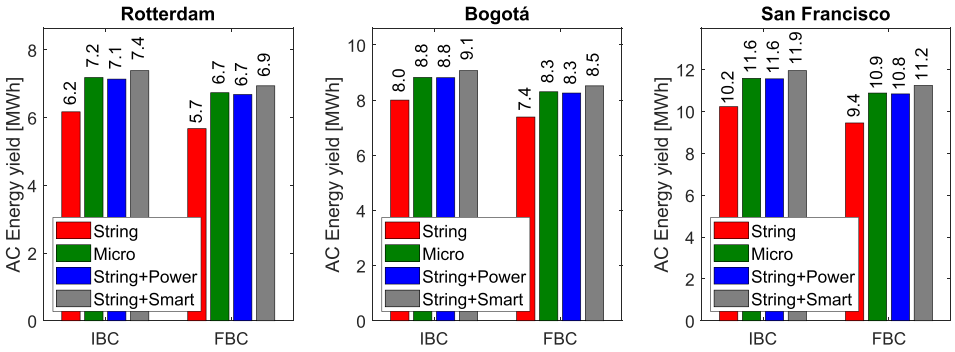


Fig. 8. The annual AC energy yield of the different PV systems across various locations. The Smart modules with string inverter have the highest yield across all locations, followed by the butterfly modules with micro inverters and the butterfly modules with power optimizers, while the most commonly used string inverters with butterfly modules are the least-performing options. Additionally, systems equipped with FBC cells perform worse than those with IBC cells.

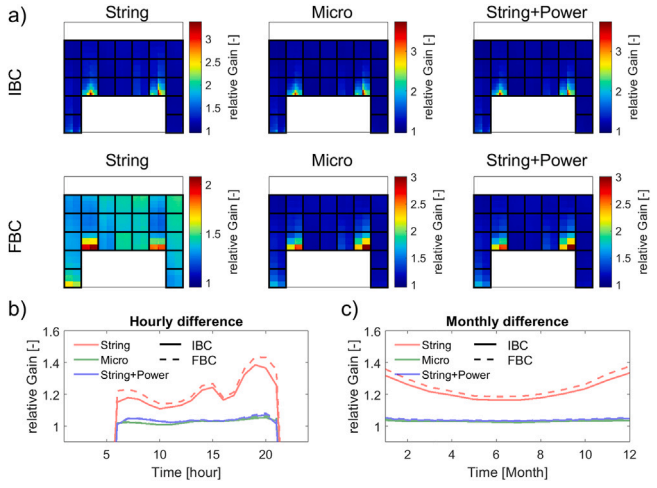


Fig. 9. (a) the annual relative gain in Rotterdam per cell for the system with Smart modules compared to the other systems. This is calculated by quantifying the annual electricity produced per cell and dividing the values of the systems. It can be seen that the cells behind the objects have the highest relative gain. (b) the relative gain in Rotterdam per hour of the day. Although the gain compared to the system with micro inverters or power optimizers is relatively constant over the day, the relative gain compared to the system with string inverters is larger at the end of the day. (c) the relative gain in Rotterdam per month for all systems. The relative gain compared to the micro and string + power system is relatively constant, whereas the gain compared to the string inverter is largest at the beginning and end of the year.

generated per cell of the system with Smart modules by that of the corresponding cell in the other systems. The largest gains are observed for cells behind the objects which face the most shading, further demonstrating the improved shade resilience of Smart modules. Only for the system with string inverters and FBC cells, is there a significant gain for all cells in the system.

In addition to the relative gain per cell, the time-dependent relative gains are also quantified. Fig. 9(b) and (c) present the relative gain as a function of the hour of the day and the month of the year, respectively. These gains are calculated by dividing the total electricity generated during a specific hour or month by the system with Smart modules by that generated by the other systems. The relative gain compared to the system with string inverters is largest toward the end of the day, as the roof has a slight westward orientation. This orientation leads to more pronounced shading patterns in the late afternoon, as illustrated in Appendix D. On a monthly basis, the gain relative to the system with string inverters is highest at the beginning and end of the year. During these months, the lower solar elevation increases shading effects, thereby enhancing the benefit of the more shade-robust Smart modules. In contrast, the relative gain compared to systems with micro inverters or power optimizers remains fairly constant throughout both the day and the year.

Lastly, it can be seen in Fig. 8 that systems with IBC cells have a higher energy yield than those with FBC cells. This difference can be attributed to the IBC cells having both higher P_{STC} and a lower reverse breakdown voltage. To separate the effect of both causes, Appendix E calculates the performance ratio of all systems. This shows that the differences between cell technologies are mostly due to the higher efficiency of the IBC solar cells. Nevertheless, the systems with IBC cells have slightly better performance ratios, demonstrating how reverse bias voltage can help mitigate partial shading, similar to the findings of Calcabrini et al. [49].

3.3. Effect on temperature

Besides the AC energy yield, temperature is also an important characteristic, as it influences degradation rates and can trigger different failure mechanisms such as hotspots [9,50,51]. Therefore, we quantify both the mean and maximum temperatures that the cells within the module experience throughout the year. Fig. 10(a) shows the spatial profile of the mean temperature of each cell in all systems in Rotterdam. The spatial profiles for other locations are shown in Appendix F, as they exhibit a similar trend, while having 2.9 °C and 4.7 °C higher mean temperatures for San Francisco and Bogotá, respectively.

The mean cell temperature heavily depends on the irradiance, showing the same spatial pattern as the received irradiation in Fig. 2. Modules located closely behind objects receive lower irradiation, leading to a lower average cell temperature. The highest temperatures are observed in the String system with modules endowed with FBC solar cells. This can be attributed to this system having both a lower shade resilience at the cell level, as well as a low shade resilience at the inverter level. To investigate how the change in mean cell temperature affects the degradation rates of the PV modules, a degradation analysis is performed in Appendix G. These results show that Smart modules have slightly lower degradation rates. However, the location of the PV system has a bigger impact on the degradation than system topology, as the received irradiance and ambient temperature heavily determine the degradation rate.

Besides the average temperature of the cells, it is also important to know the maximum temperature cells experience, as high temperatures are an important stress factor for different failure modes [9,50,51]. Fig. 10(b) shows the boxplot distribution of the maximum temperatures of all cells within the PV modules of the different systems. The

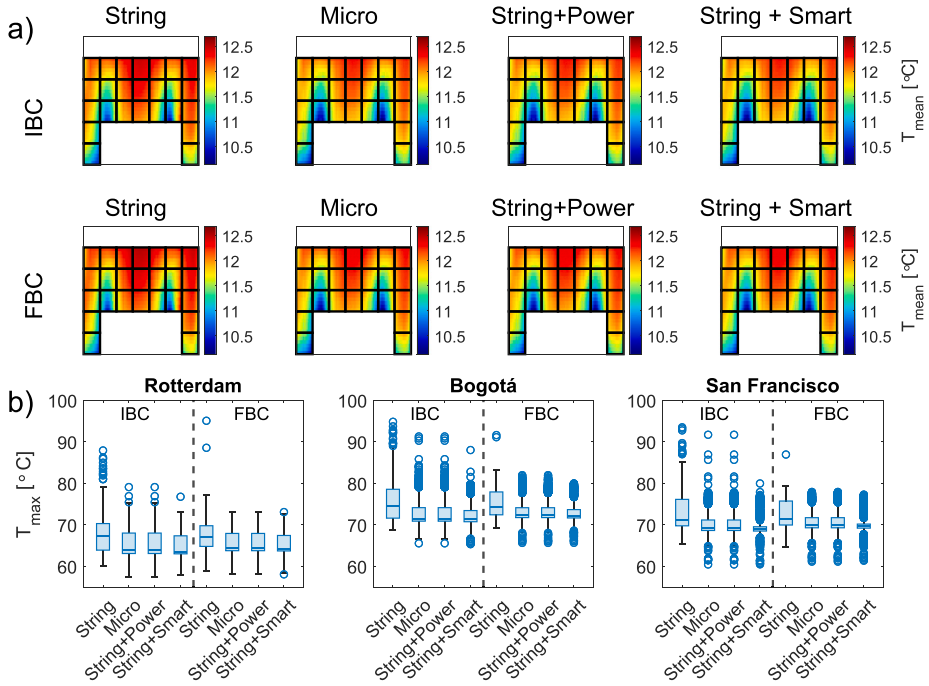


Fig. 10. (a) the mean temperature (T_{mean}) for each cell throughout the year in Rotterdam. It can be seen that T_{mean} has the same spatial profile as the received irradiance. Additionally, systems with only string inverters reach slightly higher temperatures at the top of the roof, as these systems have the lowest shade resilience. (b) the boxplot distribution of the maximum temperatures (T_{max}) of all cells within all PV modules across all locations and configurations. The smart modules reduce the maximum temperatures across all locations, as they improve the shade resilience of the PV systems.

use of Smart modules significantly reduces the maximum temperatures experienced. This is because the Smart modules improve the shade resilience of the system, leading to fewer reverse bias operations, as shown in Appendix H. Given that extreme temperatures can trigger different failure mechanisms, the Smart modules can potentially have a positive impact on the stability of the PV system. However, future work is needed to demonstrate and quantify this impact.

Interestingly, PV systems with IBC cell-endowed modules have larger extreme values than those with FBC cells. This is because the low breakdown voltage of IBC cells makes it favorable for cells to operate in reverse bias rather than activating the bypass diodes, which would occur in modules with FBC cells. Therefore, IBC cells more often operate in reverse bias, leading to higher temperatures. To support this explanation, Appendix H illustrates the fraction of time all cells are operating under reverse bias. Although all values are small, it can still be seen that IBC cells operate significantly more in reverse bias. This suggests the ideal reverse bias voltage is a trade-off between, on one hand better shade resilience and higher energy yields for low values of V_b, and on the other hand reducing extreme temperatures when V_b is high.

To quantify this trade-off, the energy yield simulations for all systems in Rotterdam are repeated with a varying V_b in Eq. (1) (while assuming all other electrical parameters to be those of the IBC cell). Fig. 11 presents the annual energy yield and maximum temperature of the different inverter topologies, showing a distinct trend for each inverter topology.

For a system with only string inverters, a low value of V_b (-5V) results in the highest energy yield and lowest T_{max}. This is in agreement with Figs. 8 and 10(b), showing a higher energy yield and lower T_{max} for the system with IBC cells when only string inverters are used. The system with micro inverters and the system with power optimizers show a maximum value for T_{max} at $V_b = 15\ V$. Still, it can be seen that a low value of V_b (-5V) has a higher T_{max} compared to larger values (-30 V to -50 V). This demonstrates the apparent trade-off, as a lower V_b does have a higher energy yield. Lastly, it can be seen that for systems with

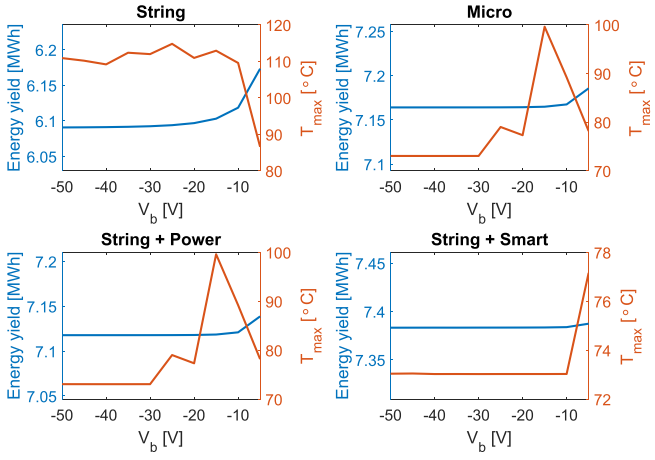


Fig. 11. The annual energy yield and maximum temperature as a function of reverse breakdown voltage for the different inverter topologies in Rotterdam.

Smart modules the performance is very similar for $V_b < -10V$. Since each substring can operate independently, cells hardly operate at reverse bias, reducing T_{max}. Only when V_b is small (-5V), reverse bias can be triggered and T_{max} increases. Although these simulations show how the energy yield and T_{max} vary for different V_b, future work is still needed to determine the optimal value, as the material properties of the solar module should also be considered.

3.4. LCOE analysis

To evaluate how the increased energy yield and the elimination of a micro-inverter or power optimizer per module affect the financial performance of the PV system with Smart modules, the LCOE is calculated

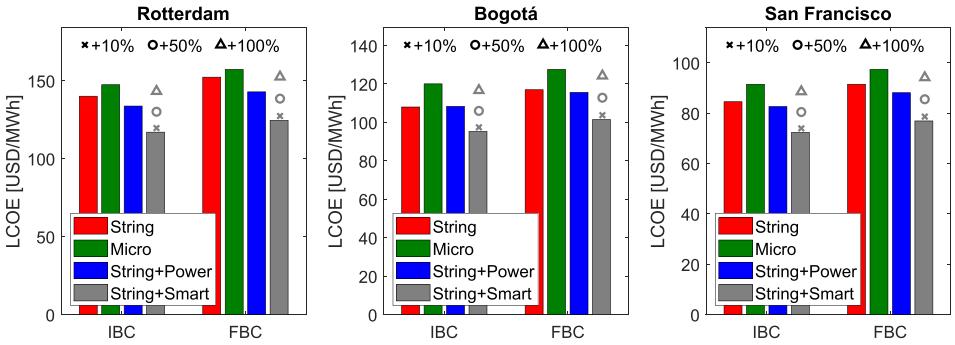


Fig. 12. The LCOE for the different systems in all locations. For the system with Smart modules, the bars do not consider additional module costs. To see how the LCOE would be affected for different module costs, three different values (i.e., 10%, 50% and 100% additional module costs) have been plotted with symbols.

for the considered systems. Fig. 12 presents the LCOE for the different systems across all locations. For the system with Smart modules, the bar plots are calculated assuming no additional module costs. The results show that, for the considered scenarios, systems equipped with Smart modules achieve a significantly lower LCOE, primarily due to the aforementioned advantages.

To assess the impact of additional module costs on this comparison, the LCOE calculation for the system with Smart modules is repeated for different cost scenarios. The symbols in Fig. 12 show the increase in LCOE corresponding to 10%, 50%, and 100% higher module costs for the Smart modules. Even with a 50% increase in module costs, the Smart module system still exhibits the lowest LCOE among all considered system topologies in all locations. It should be realized that these values may differ if other scenarios are considered. Lastly, the PV systems installed in San Francisco have the lowest LCOE as the total energy yield is the highest for this location.

4. Conclusion

In this work, we compared the performance of different PV systems to investigate the potential of Smart modules. Four different converter topologies were tested, which are butterfly modules with string inverters, butterfly modules with micro inverters, butterfly modules with power optimizers and string inverters, and Smart modules with string inverters. Additionally, two cell technologies (IBC and FBC) were included to investigate the impact of different reverse breakdown voltages. The PVMD Toolbox was employed to simulate the annual energy yield, temperature profiles, and levelized cost of electricity.

The results show that the system with Smart modules has the highest energy yield among all considered topologies, as they allow substrings to operate independently. This improved shade resilience results in a 15%–20% gain in energy yield compared to the system with string inverters, and a 2%–3% gain compared to systems with micro or power optimizers. As a result, systems with Smart modules have the lowest LCOE, with a tolerable additional module cost of at least 50% for all considered case studies. Furthermore, systems with Smart modules reduce the maximum temperatures that are observed in the system. This can potentially, although future work is needed to further demonstrate this, have a positive impact on the stability of the PV system.

To better understand the shade resilience of the PV systems, the impact of cell architecture was also examined. This shows that the reverse breakdown voltage can impose a trade-off between achieving higher energy yields (low breakdown voltage) or experiencing lower extreme temperatures (high breakdown voltage).

CRediT authorship contribution statement

Youri Blom: Writing – original draft, Software, Methodology, Investigation. **Rudi Santbergen:** Supervision. **Olindo Isabella:** Writing – review & editing, Supervision, Funding acquisition. **Malte Ruben Vogt:** Writing – review & editing, Supervision, Methodology, Funding acquisition.

Declaration of Generative AI and AI-assisted technologies in the writing process

During the preparation of this work the authors used CoPilot to paraphrase sentences and improve the language and readability. After using this tool/service, the authors reviewed and edited the content as needed and take full responsibility for the content of the publication.

Funding

This paper is partially based on results obtained from the project “Simulation study to benchmark system-level performance of Taylor Smart PV modules”, commissioned by Taylor.

Declaration of competing interest

The authors declare that they have no known competing financial interests or personal relationships that could have appeared to influence the work reported in this paper.

Acknowledgements

We want to acknowledge Timothy J. Silverman for his assistance with the financial calculations.

Appendix A. Comparison of power optimizers with micro inverters

As discussed in the introduction of the main text, the topology using power optimizers is not included in the comparison because its performance closely matches that of the micro-inverter topology. Both configurations allow each module to operate at its own maximum power point, but neither provides shade resilience between substrings.

Fig. A.1 presents the output power of both topologies for all locations and cell architectures, illustrating their strong similarity, with a maximum root mean square error (RMSE) of 0.07 kW obtained in Bogota. Most deviations occur at high output powers, where the efficiency of the micro inverter decreases as the input power approaches its rated power of 9.5 kW. This explains why Bogota has the largest RMSE, as the highest output powers are obtained for this location. Furthermore, the energy yield reported in the bottom-right corner of each plot further confirms their similar performance, with a maximum relative deviation of 0.8% for the PV system in Rotterdam with the FBC architecture.

This similarity between both topologies justifies the exclusion of one of them. Consequently, the main text focuses on the micro-inverter system for the energy yield, temperature, and degradation analyzes. However, it should be noted that a system using power optimizers exhibits comparable performance with a difference below 0.8% compared to the micro-inverter system in our simulations in these aspects.

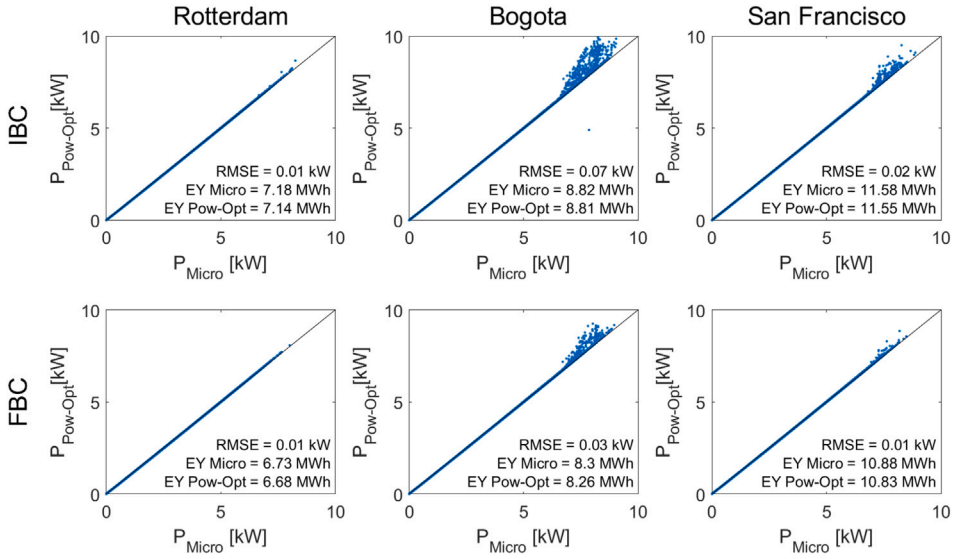


Fig. A.1. A performance comparison between the topology with power optimizers and micro inverters for all locations and cell architectures. In each plot, the output power of both systems is compared, where each point shows the produced power of both systems at a certain time of the year. It can be seen that both their power production and energy yield are very similar.

Appendix B. Validation forward bias

To validate the electrical simulation under forward bias, we compared the IV curve of the simulated module with the datasheet specifications. Fig. B.1 illustrates the IV curve of the simulated module, considering the same module dimensions reported in the datasheet. It should be noted that these module dimensions differ from the ones used in the study. Additionally, Fig. B.1 shows those IV curve characteristics of the simulated module and the from the datasheet. It can be seen that all characteristics are almost identical, validating our electrical simulation under forward bias.

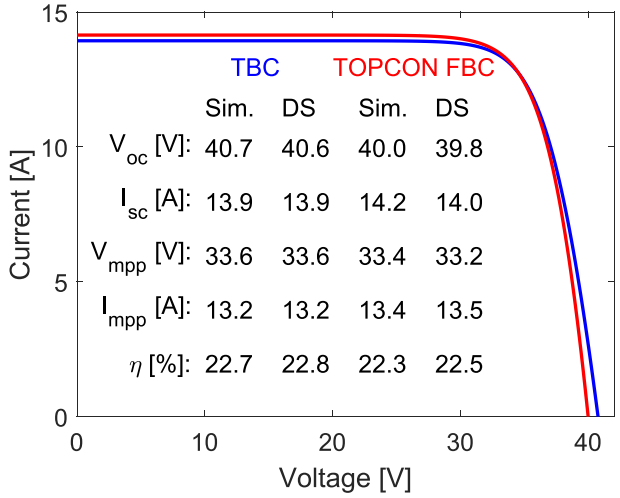


Fig. B.1. The IV curve of the simulated modules with the same module size as the datasheet, and the IV curve characteristics of both the simulated module and the datasheet. It can be seen that all characteristics are almost identical.

Appendix C. Sublevel IV curves

Fig. 7 of the main text shows the module IV curve under partial shading. To better illustrate how these module IV curves are composed of the different sublevel IV curves, Fig. C.1 shows the IV curves of the submodules. The submodules are labelled as A-I, A-II, B-I, B-II, C-I, and C-II, as shown in Fig. C.1(a). The rest of the figure displays how the submodules together construct the module IV curve.

As can be seen in the figure, the lower reverse breakdown voltage has a clear effect on the IV curve of the partially shaded submodule. This improves the performance of the module under partial shading. Additionally, it can be seen how the smart modules allow the submodules to keep their maximum power point over a wider range.

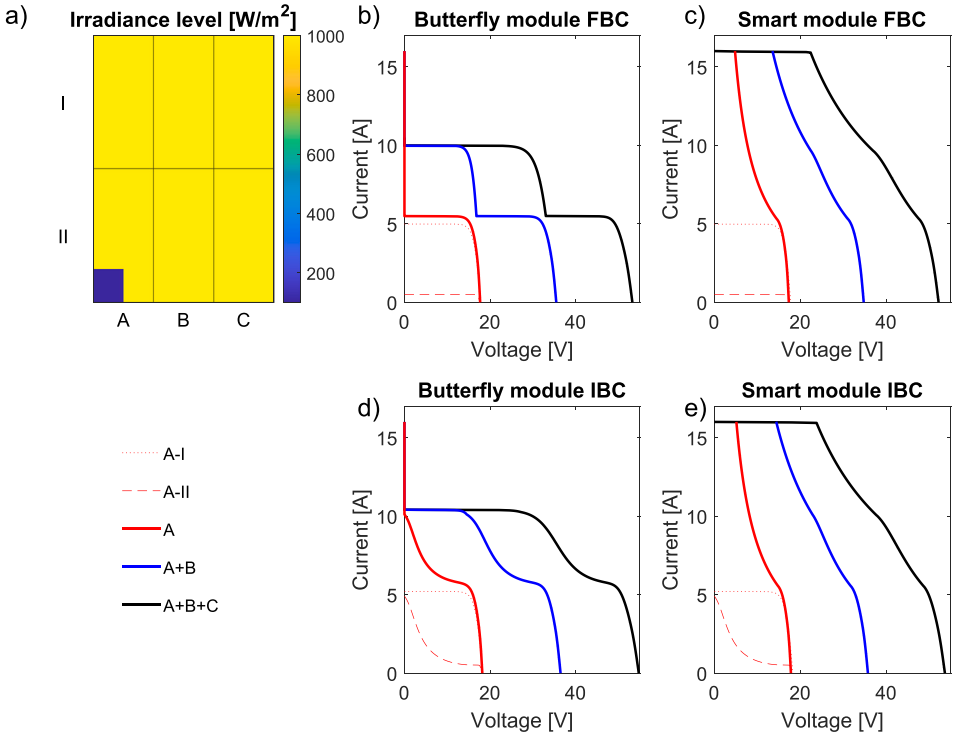


Fig. C.1. The IV curves of the different modules under a partial shading scenario. (a) shows the considered irradiance scenario. The rest of the figure shows the submodule IV curves of the butterfly module with FBC cells (b), smart modules with FBC cells (c), butterfly modules with IBC cells (d), and smart modules with IBC cells (e). In each plot, the IV curves of submodules A-I and A-II are shown. It should be noted that all other submodules have the same IV curve as A-I. It can be seen how the various submodules jointly form the module IV curve.

Appendix D. Shading pattern at throughout the day

As demonstrated in the main text, the system with Smart modules has a larger relative gain compared to the system with String inverters at the end of the day. This is because the rooftop is facing west, meaning that at the end of the day (when the sun is above the roof), there is more apparent shading in the afternoon, as demonstrated in Fig. D.1. As Smart modules improve the shade resilience of the system, the relative gain is larger at the end of the year.

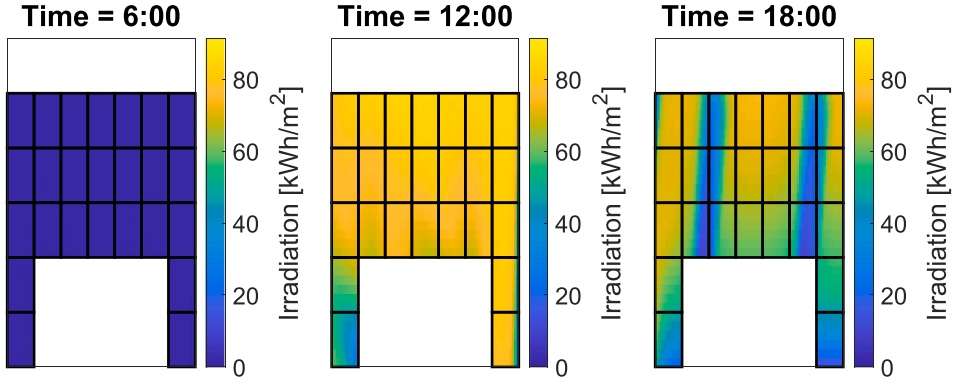


Fig. D.1. The total received irradiance for each cell at different times of the year. Due to the orientation of the roof towards the west, there is more apparent shading at the end of the day.

Appendix E. Performance ratio

The main text presents the energy yield results, showing that systems with IBC cells have a higher performance than those with FBC architecture. This difference can be attributed to the IBC cells having both higher efficiency and lower reverse breakdown voltage. To see which of these causes has a stronger impact, the performance ratio (PR) for all systems is defined as

$$PR = \frac{EY}{\sum Irr_{rec} \cdot \frac{P_{AC,STC}}{Irr_{STC}}}, \tag{E.1}$$

where EY is the energy yield, Irr_{rec} is the received irradiance across the complete PV system, $P_{AC,STC}$ is the AC system power under STC, and Irr_{STC} is the irradiance under STC (1000 W m^{-2}).

Fig. E.1 shows the PR of all systems across all locations. The difference between systems with IBC and FBC cells is smaller than in Fig. 8 as the larger efficiency for IBC cells does not have an effect on the performance ratio. This shows that the higher efficiency plays a bigger role than the lower reverse breakdown voltage. Nevertheless, systems with IBC architecture still have a slightly higher PR, meaning that their lower reverse breakdown voltage positively impacts the performance.

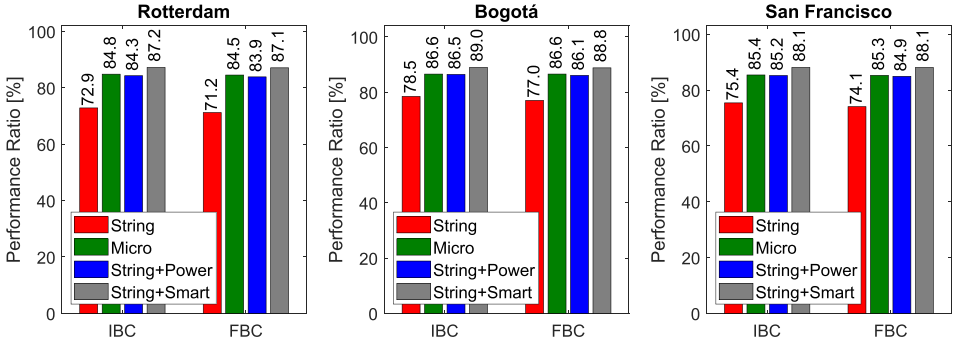


Fig. E.1. The performance ratio of the different PV systems. Systems with IBC cells have a slightly higher PR, which can be attributed to their lower reverse breakdown voltage.

Appendix F. Temperature profiles

The main text shows the spatial profile of the mean temperatures throughout the year for all systems in Rotterdam. The temperature profiles of the PV systems in Bogotá and San Francisco are shown in Fig. F.1 and Fig. F.2, respectively.

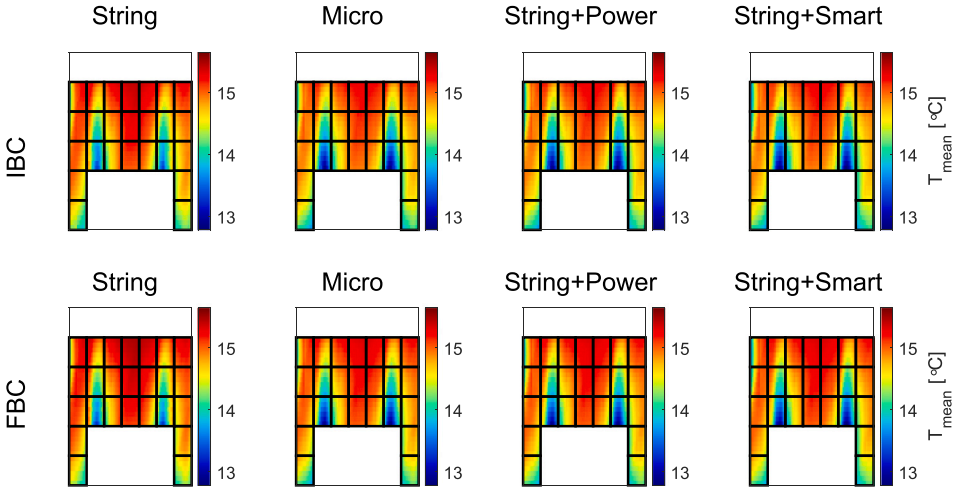


Fig. F.1. The mean temperature for each cell throughout the year in Bogotá.

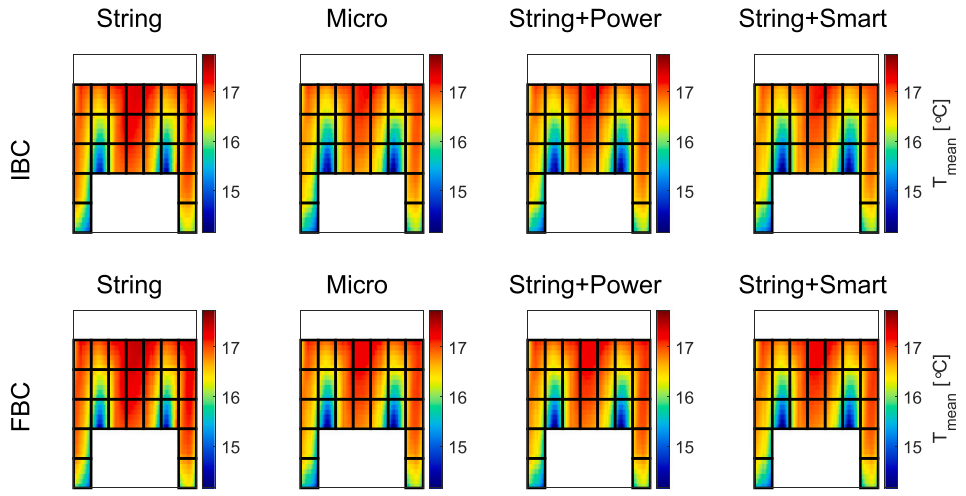


Fig. F.2. The mean temperature for each cell throughout the year in San Francisco.

Appendix G. Degradation analysis

To investigate the impact of the system topology on the degradation of the PV system, we calculate the degradation rates and the corresponding loss in energy yield of all PV systems. This Appendix section first explains the modeling of degradation rates, then discusses the calculated degradation rates, and concludes with an analysis of the robustness against degradation.

G.1. Degradation modeling

Lastly, the effect of degradation is simulated using the approach described in earlier work [52]. Three degradation mechanisms are considered, which are moisture induced degradation, discoloration, and thermal cycling. For each mechanism i, an Arrhenius-based equation is used to obtain a degradation rate $k_{deg,i}$, written as

$$k_{deg,i} = A_i \cdot (X_i)^{n_i} \cdot e^{-\frac{E_{a,i}}{k \cdot T}}, \tag{G.1}$$

where A_i is the pre-exponential constant, X_i is the stress factor corresponding to the degradation mechanism, n_i is an exponent, and $E_{a,i}$ is the activation energy. For moisture induced degradation, the related stress factor is the relative moisture concentration inside the PV module, as fully discussed in [53]. For discoloration, the stress factor is ultraviolet (UV) irradiance, while for thermal cycling, it is the number of temperature fluctuations. The full details on the calculation of the degradation rates and the implementation of their effect on the module performance are discussed in [52].

G.2. Effect on degradation

The previously mentioned temperature differences also translate into differences in power losses due to degradation, as temperature is a crucial parameter in degradation calculations. For all PV systems across various locations, the total power loss due to degradation (P_{loss}) is calculated for a lifetime, assumed to be 20 years. It should be noted that P_{loss} is calculated for each cell separately, and it does not directly relate to the overall energy yield loss of the complete PV system.

Fig. G.1(a) shows the spatial distribution of all PV systems in Rotterdam (distributions for other locations are shown in Fig. G.2 and Fig. G.3). Similar to the temperature profile, the degradation loss follows the same trend as the received irradiance. This is expected since the degradation rate depends on both the received UV irradiance and cell temperature. Overall, systems with Smart modules exhibit lower power loss compared to other PV systems.

To better quantify the differences in degradation losses, Fig. G.1(b) presents the box-plot distribution of P_{loss} values for all cells in the PV system. In all locations, systems with Smart modules and micro-inverters have significantly lower degradation losses than those with butterfly modules and string inverters. Still, Smart modules show slightly smaller extreme values compared to systems with micro-inverters.

G.3. Robustness against degradation

Lastly, we test the robustness against degradation for each system topology. The energy yield simulations are repeated, adjusting the module performance according to their calculated degradation profile. Fig. G.4 shows the change in the IV curve under STC conditions due to degradation for both the butterfly and Smart modules. It can be seen that degradation mainly results in a loss of voltage rather than a loss of current.

Fig. G.5 also shows the annual AC energy yield of all PV systems after 20 years of operation. The trends and differences are similar to those in Fig. 8, also showing the largest energy yield for the PV system with Smart modules. This indicates that all system topologies have similar robustness against degradation, as the relative differences remain consistent. These similarities can be attributed to degradation primarily affecting voltage (Fig. G.4). Since cells and modules are mostly connected in series, differences in voltage result in fewer mismatch losses compared to differences in current. The reason the higher observed values of P_{loss} for the string systems in Fig. G.1(b) do not correspond to significantly lower energy yields, is that larger values of P_{loss} do not directly correspond to a larger loss on the system level. High values for P_{loss} mostly occur for cells that receive high irradiances, meaning that these cells had been current limited by the other cells in the same string, which receive less irradiance. Thus, the

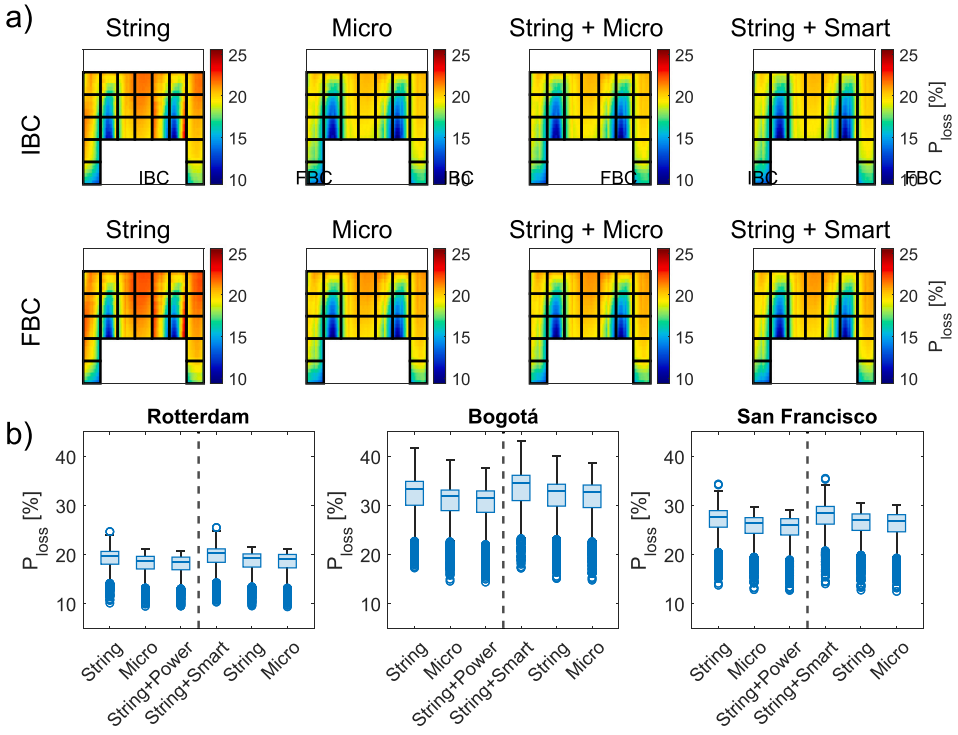


Fig. G.1. (a) the power loss due to degradation for each cell throughout the year in Rotterdam. The power losses exhibit the same spatial trend as the irradiance and mean temperature, as these heavily influence the degradation rate. (b) the boxplot distribution of the degradation losses of all cells within all PV modules over 20 years across all locations and configurations. Although there are small differences between system topologies and cell technologies, the biggest differences are due to the location.

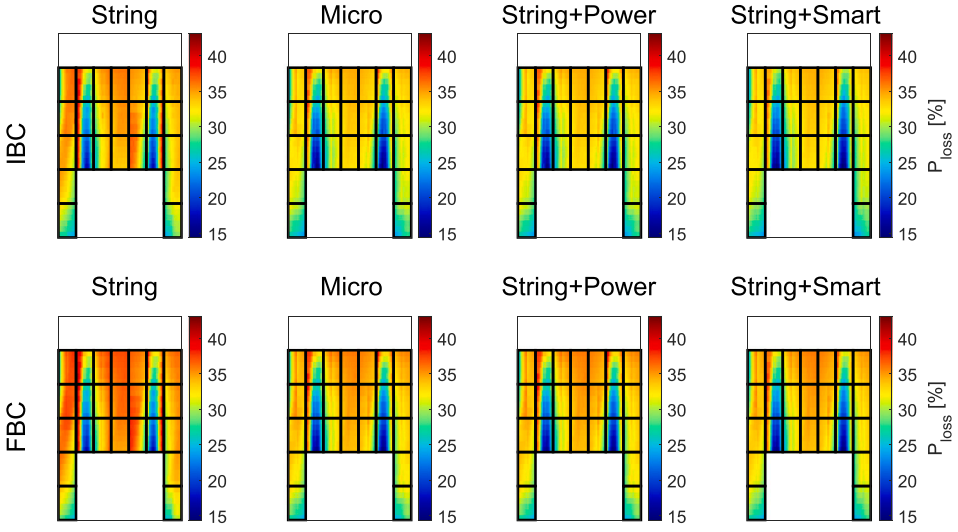


Fig. G.2. The power loss due to degradation for each cell throughout the year in Bogotá.

degradation is mostly compensated by the degraded cells having higher irradiances and the efficiency loss observed on cells with high irradiances is not strongly observed on the system energy yield level.

It can be seen, however, that the location has a significant impact on the change in energy yield. In Rotterdam, the system with smart modules with IBC cells experiences a loss in energy yield of 1.0 MWh (from 7.4 MWh to 6.4 MWh), whereas the same systems in both Bogotá and San Francisco have a loss of 2.0 MWh. This illustrates that the location has a bigger impact on the degradation than the system topology.

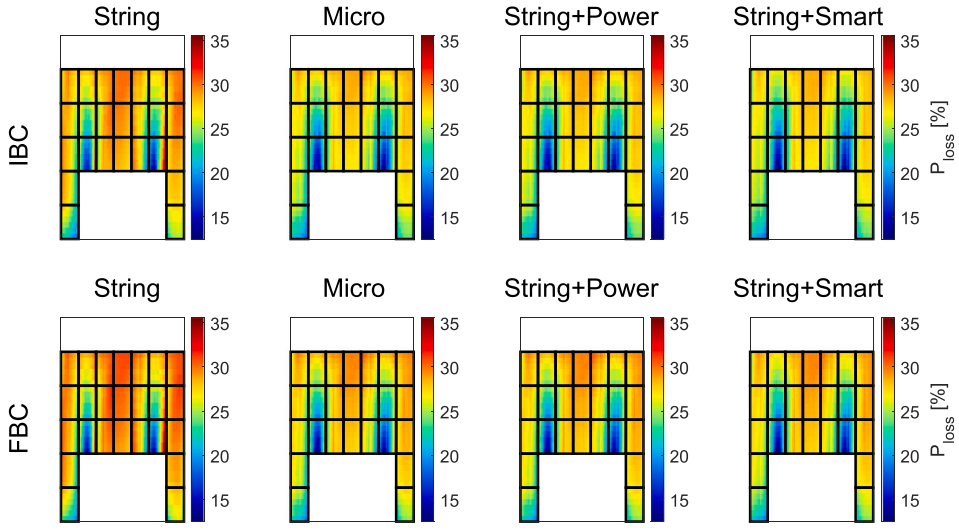


Fig. G.3. The power loss due to degradation for each cell throughout the year in San Francisco.

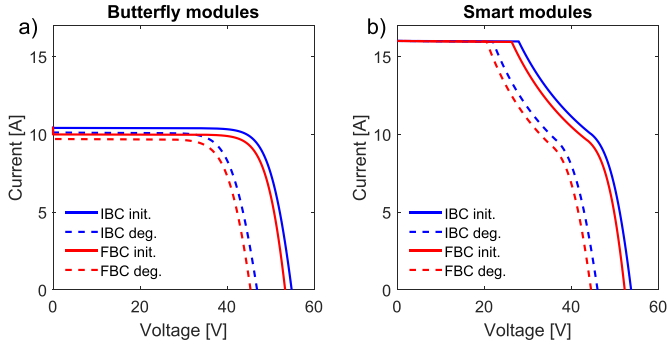


Fig. G.4. The change in module IV curve under test conditions due to degradation for the butterfly topology (a) and smart module (b) in Rotterdam. The MPP of each IV curve is indicated with a cross.

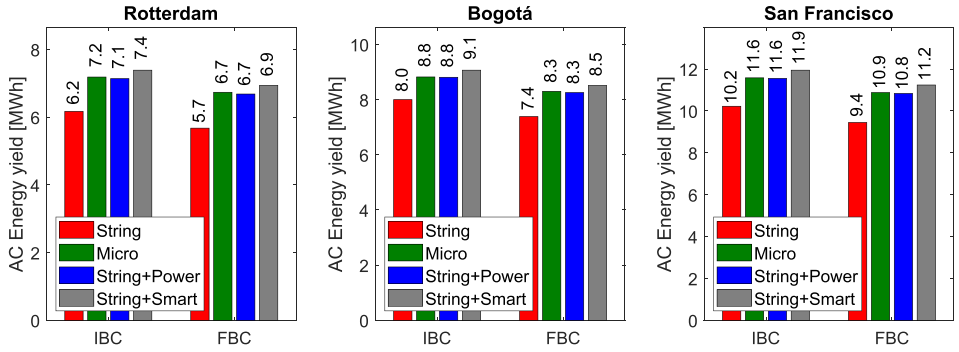


Fig. G.5. The energy yield at all locations after 20 years of degradation. The observed differences are similar to those observed for the initial energy yield.

Appendix H. Share reverse bias operation

As explained in the main text, PV systems endowed with IBC cells experience higher extreme temperatures, as IBC cells operate more frequently at reverse bias. To support this explanation, Fig. H.1 shows the relative share of time that the cells in a PV system are operating at reverse bias.

It can be seen that in each location, PV systems with string inverters and IBC cells operate the most time at reverse bias, reaching values up to 0.82%. Although all values are small, it can be seen that there are significant differences among the simulated PV systems.

These larger values for PV systems with IBC cells can explain why these systems experience higher extreme temperatures. As heat is injected into the cell when operating at reverse bias, high temperatures are more likely to occur for IBC cells.

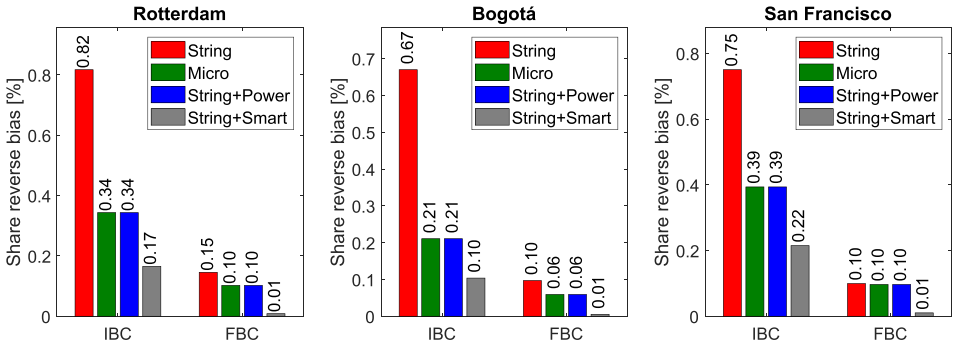


Fig. H.1. The relative share at which cells in a PV system are operating under reverse bias. The numbers throughout these figures represent the percentage of time cells operate under reverse bias in the year.

Data availability

Data will be made available upon request.

References

[1] D.M. Kammen, D.A. Sunter, City-integrated renewable energy for urban sustainability, Science 352 (6288) (2016) 922–928, https://doi.org/10.1126/science.aad9302

[2] A. Ahmed, T. Ge, J. Peng, W.-C. Yan, B.T. Tee, S. You, Assessment of the renewable energy generation towards net-zero energy buildings: a review, Energy Build. 256 (2022) 111755, https://doi.org/10.1016/j.enbuild.2021.111755, https://www.sciencedirect.com/science/article/pii/S0378778821010392.

[3] M.K. Basher, M. Nur-E-Alam, M.M. Rahman, K. Alameh, S. Hinckley, Aesthetically appealing building integrated photovoltaic systems for net-zero energy Buildings. Current status, challenges, and future developments—a review, Buildings 13 (4) (2023), https://doi.org/10.3390/buildings13040863, https://www.mdpi.com/2075-5309/13/4/863.

[4] C. S. Netherlands, Most solar panels installed at commercial premises, 2025, https://www.cbs.nl/en-gb/news/2025/32/most-solar-panels-installed-at-commercial-premises (Last accessed 4 November 2025).

[5] C.S. Netherlands, Consumption of energy from renewable sources rises to 20 percent, 2025, https://www.cbs.nl/en-gb/news/2025/23/consumption-of-energy-from-renewable-sources-rises-to-20-percent (Last accessed 4 November 2025).

[6] O.A. Arráez-Cancelliere, N. Muñoz-Galeano, J.M. Lopez-Lezama, Performance and economical comparison between micro-inverter and string inverter in a 5, 1 kWp residential PV-system in Colombia, in: 2017 IEEE Workshop on Power Electronics and Power Quality Applications (PEPQA), 2017, pp. 1–5, https://doi.org/10.1109/PEPQA.2017.7981678

[7] D. Sailor, J. Anand, R. King, Photovoltaics in the built environment: a critical review, Energy Build. 253 (2021) 111479, https://doi.org/10.1016/j.enbuild.2021.111479, https://www.sciencedirect.com/science/article/pii/S0378778821007635.

[8] B. Yang, H. Ye, J. Wang, J. Li, S. Wu, Y. Li, H. Shu, Y. Ren, H. Ye, PV arrays reconfiguration for partial shading mitigation: recent advances, challenges and perspectives, Energy Convers. Manag. 247 (2021) 114738, https://doi.org/10.1016/j.enconman.2021.114738, https://www.sciencedirect.com/science/article/pii/S0196890421009146.

[9] S. Tang, Y. Xing, L. Chen, X. Song, F. Yao, Review and a novel strategy for mitigating hot spot of PV panels, Sol. Energy 214 (2021) 51–61, https://doi.org/10.1016/j.solener.2020.11.047, https://www.sciencedirect.com/science/article/pii/S0038092X20312068.

[10] S. Harb, M. Kedia, H. Zhang, R.S. Balog, Microinverter and string inverter grid-connected photovoltaic system — a comprehensive study, in: 2013 IEEE 39th Photovoltaic Specialists Conference (PVSC), 2013, pp. 2885–2890, https://doi.org/10.1109/PVSC.2013.6745072

[11] M.S. Tariq, S.A. Butt, H.A. Khan, Impact of module and inverter failures on the performance of central-, string-, and micro-inverter PV systems, Microelectron. Reliab. 88-90 (2018) 1042–1046, 29th European Symposium on Reliability of Electron Devices, Failure Physics and Analysis (ESREF 2018). https://doi.org/10.1016/j.microrel.2018.06.096, https://www.sciencedirect.com/science/article/pii/S002627141830516X.

[12] D. Feldman, V. Ramasamy, R. Fu, A. Ramdas, J. Desai, R. Margolis, U.S. Solar Photovoltaic System and Energy Storage Cost Benchmark (Q1 2020), National Renewable Energy Lab. (NREL), Golden, CO (United States) Jan 2021, https://doi.org/10.2172/1764908. https://www.osti.gov/biblio/1764908., Tech. rep.

[13] C. Kost, Study: Levelized Cost of Electricity- Renewable Energy Technologies, Tech. rep, Fraunhofer ISE, 2024.

[14] E. Roman, R. Alonso, P. Ibanez, S. Elorduizapatarietxe, D. Goitia, Intelligent PV module for grid-connected PV systems, IEEE Trans. Ind. Electron. 53 (4) (2006) 1066–1073, https://doi.org/10.1109/TIE.2006.878327

[15] S.M. MacAlpine, R.W. Erickson, M.J. Brandemuehl, Characterization of power optimizer potential to increase energy capture in photovoltaic systems operating under nonuniform conditions, IEEE Trans. Power Electron. 28 (6) (2013) 2936–2945, https://doi.org/10.1109/TPEL.2012.2226476

[16] J.L. de Souza Silva, H.S. Moreira, M.V.G. dos Reis, T.A. dos Santos Barros, M.G. Villalva, Theoretical and behavioral analysis of power optimizers for grid-connected photovoltaic systems, Energy Rep. 8 (2022) 10154–10167, https://doi.org/10.1016/j.egyr.2022.07.154, https://www.sciencedirect.com/science/article/pii/S2352484722014196.

[17] B. Passarella, M. Verkou, M. Leonardi, F. Coco, Y. Blom, M. Vogt, R. Santbergen, A. Di Stefano, A. Canino, M. Foti, A. Ragonesi, M. Sciuto, F. Rametta, M. Zeman, O. Isabella, C. Gerardi, Partial shading of photovoltaic modules: a comparison between simulated and measured IV characteristics, in: 2023 IEEE 50th Photovoltaic Specialists Conference (PVSC), 2023, pp. 1–3, https://doi.org/10.1109/PVSC48320.2023.10359834

[18] D. Mathew, J. P. Ram, Y.J. Kim, Unveiling the distorted irradiation effect (Shade) in photovoltaic (PV) power conversion – a critical review on Causes, Types, and its minimization methods, Solar Energy 266 (2023) 112141, https://doi.org/10.1016/j.solener.2023.112141, https://www.sciencedirect.com/science/article/pii/S0038092X23007752.

[19] L. Fauzan, M.J. Yun, Y.H. Sim, D.Y. Lee, S.I. Cha, Small area high voltage photovoltaic module for high tolerance to partial shading, iScience 26 (6) (2023) 106745, https://doi.org/10.1016/j.isci.2023.106745, https://www.sciencedirect.com/science/article/pii/S2589004223008222.

[20] L. Fauzan, Y.H. Sim, M.J. Yun, H. Choi, D.Y. Lee, S.I. Cha, Power from shaded photovoltaic modules through bypass-diode-assisted small-area high-voltage structures, Renew. Sustain. Energy Rev. 208 (2025) 115047, https://doi.org/10.1016/j.rser.2024.115047, https://www.sciencedirect.com/science/article/pii/S1364032124007731.

[21] O. Khan, W. Xiao, Review and qualitative analysis of submodule-level distributed power electronic solutions in PV power systems, Renew. Sustain. Energy Rev. 76 (2017) 516–528, https://doi.org/10.1016/j.rser.2017.03.073, https://www.sciencedirect.com/science/article/pii/S1364032117304094.

[22] S. Sarwar, M.Y. Javed, M.H. Jaffery, M.S. Ashraf, M.T. Naveed, M.A. Hafeez, Modular level power electronics (MLPE) based distributed PV system for partial shaded conditions, Energies 15 (13) (2022), https://doi.org/10.3390/en15134797, https://www.mdpi.com/1996-1073/15/13/4797.

[23] D.A. van Nijen, P. Manganiello, M. Zeman, O. Isabella, Exploring the benefits, challenges, and feasibility of integrating power electronics into c-Si solar cells, Cell Rep. Phys. Sci. 3 (7) (Jul 2022), https://doi.org/10.1016/j.xcrp.2022.100944

[24] M.E.T. Souza Junior, L.C.G. Freitas, Power electronics for modern sustainable power systems: distributed generation, microgrids and smart grids—a review, Sustainability 14 (6) (2022), https://doi.org/10.3390/su14063597, https://www.mdpi.com/2071-1050/14/6/3597.

[25] A. Calcabrini, M. Muttillo, R. Weegink, P. Manganiello, M. Zeman, O. Isabella, A fully reconfigurable series-parallel photovoltaic module for higher energy yields in urban environments, Renew. Energy 179 (2021) 1–11, https://doi.org/10.1016/j.renene.2021.07.010, https://www.sciencedirect.com/science/article/pii/S0960148121010156.

[26] J.T. Stauth, M.D. Seeman, K. Kesarwani, Resonant switched-capacitor converters for sub-module distributed photovoltaic power management, IEEE Trans. Power Electron. 28 (3) (2013) 1189–1198, https://doi.org/10.1109/TPEL.2012.2206056

[27] S.Z. Mirbagheri Golroodbari, A.C. De Waal, W.G.J.H.M. Van Sark, Improvement of shade resilience in photovoltaic modules using buck converters in a smart module architecture, Energies 11 (1) (2018), https://www.mdpi.com/1996-1073/11/1/250.

[28] S.Z.M. Golroodbari, A.C. de Waal, W.G. van Sark, Proof of concept for a novel and smart shade resilient photovoltaic module, IET Renew. Power Gener. 13 (12) (2019) 2184–2194, https://doi.org/10.1049/iet-rpg.2018.6127

[29] TaylorSolar, Taylor. https://www.taylor.solar/?r=0 (Accessed on 5 January 2026).

[30] M. Vogt, C.R. Tobon, A. Alcañiz, P. Procel, Y. Blom, A.N. El Din, T. Stark, Z. Wang, E.G. Goma, J. Etxebarria, H. Ziar, M. Zeman, R. Santbergen, O. Isabella, Introducing a comprehensive physics-based modelling framework for tandem and other PV systems, Sol. Energy Mater. Sol. Cells

247 (2022) 111944, https://doi.org/10.1016/j.solmat.2022.111944, https://www.sciencedirect.com/science/article/pii/S0927024822003622.
[31] Y. Blom, M.R. Vogt, O. Isabella, R. Santbergen, Improving the comprehensive modeling framework for various novel photovoltaic systems, Adv. Theory Simul. 9 (5) (2026) e01793, https://doi.org/10.1002/adts.202501793.
[32] Delft High Performance Computing Centre (DHPC), DelftBlue supercomputer (phase 2), 2024, https://www.tudelft.nl/dhpc/ark:/44463/DelftBluePhase2.
[33] P. Procel, Y. Zhou, M. Verkou, M. Leonardi, D. Di Girolamo, G. Giuliano, O. Dupré, Y. Blom, M. Vogt, R. Santbergen, F. Rametta, M. Foti, C. Gerardi, M. Zeman, O. Isabella, PV multiscale modelling of perovskite / silicon two-terminal devices: from accurate cell performance simulation to energy yield prediction, Sol. Energy Mater. Sol. Cells 293 (2025) 113864, https://doi.org/10.1016/j.solmat.2025.113864, https://www.sciencedirect.com/science/article/pii/S0927024825004659.
[34] A. Calcabrini, R. Weegink, P. Manganiello, M. Zeman, O. Isabella, Simulation study of the electrical yield of various PV module topologies in partially shaded urban scenarios, Sol. Energy 225 (2021) 726–733, https://doi.org/10.1016/j.solener.2021.07.061, https://www.sciencedirect.com/science/article/pii/S0038092X21006381.
[35] N. Klasen, F. Lux, J. Weber, T. Roessler, A. Kraft, A comprehensive study of module layouts for silicon solar cells under partial shading, IEEE J. Photovolt. 12 (2) (2022) 546–556, https://doi.org/10.1109/JPHOTOV.2022.3144635
[36] D. Solar, N-Type MONO-FACIAL MODULE https://www.solease.nl/app/uploads/2024/07/Datasheet-DMEGC-DMXXXM10RT-54HBB.pdf (Last accessed 24 February 2025)., Model = DM450M10RT-54HBB.
[37] AIKO, N-Type ABC Mono-glass module https://static.groothandelsolar.com/downloads/2024/03/08/aiko-65eae936eb475477071316.pdf (Last accessed 24 February 2025)., Model = AIKO-A460-MAH54Mb.
[38] M. Alonso-García, J. Ruíz, Analysis and modelling the reverse characteristic of photovoltaic cells, Sol. Energy Mater. Sol. Cells 90 (7) (2006) 1105–1120, https://doi.org/10.1016/j.solmat.2005.06.006, https://www.sciencedirect.com/science/article/pii/S0927024805002199.
[39] C. Reichel, J. Forster, B. Artha, K. Ingwersen, A. Tummalieh, J. Weber, E. Fokuhl, L.C. Rendler, D.H. Neuhaus, Design aspects in consideration of hotspot phenomena in high-performance photovoltaic modules featuring different silicon solar cell architectures, Sol. Energy Mater. Sol. Cells 276 (2024) 113058, https://doi.org/10.1016/j.solmat.2024.113058, https://www.sciencedirect.com/science/article/pii/S0927024824003702.
[40] C.E. Clement, J.P. Singh, E. Birgersson, Y. Wang, Y.S. Khoo, Illumination dependence of reverse leakage current in silicon solar cells, IEEE J. Photovolt. 11 (5) (2021) 1285–1290, https://doi.org/10.1109/JPHOTOV.2021.3088005
[41] W.E. Boyson, G.M. Galbraith, D.L. King, S. Gonzalez, Performance Model for Grid-Connected Photovoltaic Inverters, Sandia National Laboratories (SNL), Albuquerque, NM, and Livermore, CA (United States) Sep 2007, https://doi.org/10.2172/920449. https://www.osti.gov/biblio/920449., Tech. rep.
[42] ENPHASE, IQ8 series microinverters https://enphase.com/nl-nl/download/\protect\penalty-\@Miq8-series-microinverters-datablad?srsltid=AfmBOoqYFxjCuJNWB0Grcylm0brzWnOaIfDyPZmEAuJ5WRcf4jMq8Dsh (Last accessed 28 February 2025)., Model = IQ8HC-72-M-INT.
[43] F. ESS, T serie (g3) 3-fase omvormers https://nl.fox-ess.com/wp-content/uploads/2023/03/NL-TG3-datasheet-3.6.pdf (Last accessed 28 February 2025)., Model = T12-G3.
[44] StralendGroen, SolarEdge power optimizer S500 https://www.stralendgroen.\protect\penalty-\@Mnl/product/solaredge-power-optimizer-s500/?srsltid=AfmBOopRFbQeDinQ9RtzYr1VAHjEbAEyhNBkjxXA8T9hSyczj2crOTpF&v=1a13105b7e4e (Last accessed 17 April 2026).
[45] IRENA, Renewable power generation costs in 2024, Jul 2025, https://www.irena.org/Publications/2025/Jun/Renewable-Power-Generation-Costs-in-2024.
[46] Elektrototaalmarkt, Foxess t3-g3 afci + wifi omvormer 3f 3kw afci wifi g3 https://www.elektrototaalmarkt.nl/4211118?gad_source=1&gad_campaignid=17680007513&gbraid=0AAAAD9IGgP3JPVxz9H3BFmHu8wHgZLP4&gclid=CjwKCAjw7vzOBhBxEiwAc7WNr5EE2FmtuT5-1oY1_jlx1LMxY1-_vMyOc-BfkBlKOtZ2uRsFIKv8SxoCjjAQAvD_BwE (Last accessed 15 April 2026).
[47] Enphase, IQ8HC microinverter https://enphase.com/store/microinverters/iq8-series/iq8hc-microinverter (Last accessed 15 April 2026).
[48] L. Deville, M. Theristis, K.S. Anderson, 2023 PVPMC Blind Modeling Comparison Update, Tech. rep, Sandia National Lab.(SNL-NM), Albuquerque, NM (United States), 2024.
[49] A. Calcabrini, P. Procel Moya, B. Huang, V. Kambhampati, P. Manganiello, M. Muttillo, M. Zeman, O. Isabella, Low-breakdown-voltage solar cells for shading-tolerant photovoltaic modules, Cell Rep. Phys. Sci. 3 (12) (2022) 101155, https://doi.org/10.1016/j.xcrp.2022.101155
[50] G. Goudelis, P.I. Lazaridis, M. Dhimish, A review of models for photovoltaic crack and hotspot prediction, Energies 15 (12) (2022), https://doi.org/10.3390/en15124303, https://www.mdpi.com/1996-1073/15/12/4303.
[51] L.M. Shaker, A.A. Al-Amiery, M.M. Hanoon, W.K. Al-Azzawi, A.A.H. Kadhum, Examining the influence of thermal effects on solar cells: a comprehensive review, Sustain. Energy Res. 11 (1) (2024) 6, https://doi.org/10.1186/s40807-024-00100-8
[52] Y. Blom, R. Santbergen, O. Isabella, M. Ruben Vogt, Combining Physical- and Scenario-Based Modeling to Identify Tolerable Degradation Rates for Perovskite in Perovskite/Silicon Tandem Modules, Manuscript in Preparation 2025.
[53] Y. Blom, D. Jimenez Pelarda, T. Minett, I. Kaaya, N. Kyranaki, R. Santbergen, O. Isabella, M. Ruben Vogt, Modelling moisture ingress in PV modules with different encapsulant and backsheet materials, Renew. Energy 252 (2025).